2

2.2

Imaging the source region of the 2004 mid-Niigata prefecture earthquake and the evolution of a seismogenic thrust-related fold

Aitaro Kato, Eiji Kurashimo, Naoshi Hirata, Shinichi Sakai, Takaya Iwasaki, Toshihiko Kanazawa

Earthquake Research Institute, University of Tokyo, Tokyo, Japan.

Abstract The velocity structure and accurate aftershock distributions of the 2004 mid-Niigata prefecture earthquake are elucidated by inverting the arrival times from 716 aftershocks using double-difference tomography. Fourteen temporal seismic stations were immediately deployed in and around the source region within 46 h of the occurrence of mainshock. The seismic velocities in a hanging wall are lower than those in a footwall, and the velocity contrast extends to a depth of approximately 10 km. The aftershocks associated with the mainshock are distributed around the clear boundary between the low and high velocity structures. It is interpreted that the mainshock fault plane of the mid-Niigata prefecture earthquake was reactivated as a reverse fault since the crustal shortening initiated at 3.5 Ma. Crustal stretching or shortening along the Japan coastline has created complex structures such as low velocity zones, which can potentially control the seismic activities around the source region.

Key words: tomography, velocity structure, mid Niigata prefecture earthquake, aftershocks

1. Introduction

A shallow M_w 6.6 inland earthquake occurred in northwestern Japan (Niigata prefecture) on October 23, 2004, and caused serious seismic damages including landslides in the surrounding areas. The focal mechanism of this earthquake is the reverse fault type with a strike of approximately N35E (Fig. 1). It should be noted that the number of large aftershocks (M > 4) is significantly greater than other inland earthquakes [Japan Meteorological Agency (JMA) catalog] that have

recently occurred in Japan. The sequence of aftershocks with magnitudes greater than 4 continued for approximately 2 weeks after the occurrence of the mainshock. The reason for such a long sequence of aftershocks with large magnitude is difficult to be understood. Geological studies indicate that the surface folding was well developed around the source region since 3.5 Ma, following the extension stage of the Japan Sea [*Sato,* 1994]. Thus, the complex structures, associated with both the crustal stretching and the folding, can potentially nucleate the mainshock and trigger a sequence of large aftershocks. Therefore, it is important to image the complex seismogenic structures around the source region and clarify their relation to the rupture process [*e.g., Hauksson et al.,* 2004].

In Japan, although a dense seismic telemetry network has been deployed by the NIED (National Research Institute for Earth science and Disaster Prevention), JMA, and universities, the average spacing of the stations (approximately 20 km) is not sufficient to resolve even the dips of the fault planes due to the mainshock and some large aftershocks. It is also crucial to immediately collect data on aftershocks, since the rate of aftershocks rapidly decays with elapsed time (obeying the Ohmori law) and both aftershock distribution and velocity structure vary with elapsed time [*e.g., Li and Vidale,* 2001]. In order to investigate the accurate distribution of aftershocks and the velocity structure in and around the source region immediately after the occurrence of the mainshock, we began to deploy temporary seismic stations around the mainshock area from Oct. 24 and finally established 14 temporary stations within 46 h of the occurrence of the mainshock. These data would provide us with the necessary information for understanding the occurrence of the aftershock sequence and synthesizing seismotectonics. In this paper, we performed seismic tomography around the source region using the data on the aftershocks collected immediately after the mainshock, and we discuss the relationship between the three-dimensional velocity structure and the earthquake generation process.

2. Data and methods

Figure 1 shows the map of the seismic stations, the epicenters of relocated aftershocks, and the grids for the tomography used in this study. The seismic network consists of the 14 temporary stations with 3 components and 28 permanent stations located less than 70 km from the center of the source region (some of them are not shown in the figure). Each temporary seismic station was equipped with a 1-Hz seismometer, signals of which were recorded continuously at a sampling rate of 100 Hz. Both P- and S-wave arrival times observed at the temporary and permanent stations were picked manually. Then, the double-difference tomography method [*Zhang and Thurber,* 2003] was applied to the P- and S-wave data. The double difference denotes the difference between the observed and calculated travel time of two events obtained at a particular station. The double difference data enable us to determine the velocity structure of not only the entire area covered by the ray but also the detailed structures around the hypocenters. In this analysis, we selected the hypocenters of the 716 aftershocks that occurred from 2000h on Oct. 24 to 1000h on Oct. 27 from the JMA catalog. The magnitude of most of the aftershocks considered in this study was greater than 1.6. The initial hypocenter locations are determined assuming two different 1D velocity structures of the northwestern and southeastern sides of the source region (Table 1). The boundary between these velocity structures roughly coincides with that of the Muikamachi fault (Fig. 1) and its northeastward extension. The two velocity structures were chosen based on a refraction study conducted approximately 20 km south of the source region [*Takeda et al,* 2005], the geological map [GSJ, 2002], and the Bouguer gravity anomaly [GSJ, 2000]. At shallow depths of less than 3 km, the northwestern side of the Muikamachi fault has a significant low velocity, while the southeastern side has a moderately high velocity. The initial velocity structure for the tomography analysis is the same as for hypocenter determinations (Table 1), and the V_p/V_s value is set as 1.73 in all the grids. The absolute arrival times for the P- and S-wave used in the tomography are 19,656 and 19,171, respectively, and the sum of the double-difference data for the P- and S-wave reaches 300,542. The

grids are located at –300, –15, –10, –6, –3, 0, 3, 6, 10, 15, and 300 km on the X (N125E) axis; –300, –20, –15, –10, –5, 0, 5, 10, 15, 20, and 300 km on the Y (N35E) axis; and –150, 0, 3, 6, 9, 12, 15, 20, and 300 km on the Z (depth) axis (Fig. 1). Different smoothing weights 1, 5, 10, and 15 were tested. The main features of these models are very similar in the regions with good ray coverage. Considering the trade off between the roughness and the stabilization of the model [*Zhang and Thurber,* 2003], we chose the model using weight 10 as our preferred model. The weighted root mean square (RMS) travel time residual was reduced from 0.276 s to 0.061 s after 20 iterations. The relocated cluster centroid shifted by approximately 350 m in the horizontal southwestward direction and 110 m in the vertical direction.

3. Tomographic images

Figure 2 shows the P-wave velocity (V_p) structures along four cross sections perpendicular to the fault strike along with the relocated aftershocks. From the aftershock distributions, it was determined that the mainshock and the largest aftershock occurred on the two westward dipping planes that were at an angle of 60° and about 5 km away; on the other hand, the aftershock on Oct. 27 occurred on the eastward dipping plane that was at an angle of 25°, which is conjugate to the main fault. The dip angles of the three events are consistent with those of the focal mechanisms. The white-masked areas in the velocity structure correspond to the low model resolution evaluated by the following two synthetic tests. First, the travel times were calculated with a checkerboard model, alternating high- and low-velocity anomalies with 5% in the three spatial directions. Then, the synthetic data were inverted with a laterally homogeneous starting model. The unmasked areas in the figures correspond to the areas where the inverted synthetic model shows good recovery of the initial anomalies. Second, the restoring resolution test [*Zhao et al.,* 1992] was performed. The travel times were calculated using the obtained velocity structure with random noises of 0.05 s and 0.1 s for the P-wave and S-wave, respectively. The inverted model, which was initially a

homogeneous structure, has almost the same structure as the original one in the unmasked areas. Further, we checked the distributions of the derivative weight sum (DWS) values [*Zhang and Thurber*, 2003]. The DWS values indicate the sum of the partial derivatives of the velocity at each grid, and it may be a good indicator of the model resolution. The unmasked area coincides with high DWS values—greater than 500. Thus, it is demonstrated that the unmasked areas in each cross section of the velocity structure are well resolved.

It is found from Figure 2 that the P-wave velocities in the hanging wall are lower than those in the footwall in all of the four cross sections, and the velocity contrast extends to a depth of approximately 10 km. The depth extent of the low velocity body in the hanging wall is more significant on the southern cross sections (Y = –5, 0 km) than on the northern ones (Y = 5, 10 km). It should be noted that the aftershocks associated with the mainshock fault plane are distributed around the structural boundary between the low and high velocity bodies except on the Y = 5 km cross section (Fig. 2b). On the Y = 5 km cross section, the number of aftershocks is lower than those on the other cross sections, and the high velocity body is imaged around the mainshock fault plane. Further, the activities of the aftershocks associated with the largest aftershock (westward dipping plane) are limited to depths greater than 4 km. The shallow high velocity body was imaged above the upper cutoff of this seismicity (Fig. 2b, 2c). Thus, it is suggested that the seismic activities around the source region are suppressed by the high velocity body, which functions as a seismic barrier [*Aki,* 1979].

It is observed that the hypocenter of the mainshock coincides with the low V_p zone (Fig. 2c). Further, it is interesting to note that that both the largest and eastward dipping aftershocks (Oct. 27) occurred in the slightly low V_p zones in the footwall of the high velocity body (Fig. 2a, 2b).

Figure 3 shows the distributions of the ratio of V_p to the S-wave velocity (V_s) on the Y = 5 km cross section, where the S-wave structure is most widely resolved among the four cross sections. The areas with a high resolution for V_s are smaller than those with a high resolution for V_p because

of the larger errors associated with the S-wave picks. This figure shows that the body with a high V_p/V_s value is located in the hanging wall, while the footwall generally exhibits a lower V_p/V_s value. The aftershocks are distributed in the low-to-moderate V_p/V_s zone, and the significantly low V_p/V_s zone coincides with the area where the aftershock activity is low.

4. Discussion and conclusions

Figures 2(a)–(d) show that the aftershock distribution, which might be triggered by the mainshock, kinks at a depth of approximately 5 km. The inclination of the fault plane reduces above 5 km, and the fault plane extends to the surface trace of the Obiro fault or the Muikamachi fault (Fig. 1). The Muikamachi fault is a structural boundary between the western Niigata basin and the eastern basement older than 30 Ma [*e.g., Sato,* 1994]. Although the aftershock distribution indicates that the dynamic shear rupture extended to the shallower fault with a low dip angle, an obvious surface fault slip along the fault has not yet been observed.

The seismic images obtained in this study illustrate that the velocity contrast between the hanging wall and the footwall extends to a depth of 10 km. The high velocity body with a low V_p/V_s value imaged in the footwall is considered to be the old basements. In contrast, the low velocity body with a high V_p/V_s value in the hanging wall corresponds to the sediments (larger than 6 km in thickness) that have piled over the half grabens formed by crustal stretching in the opening of the Japan Sea. Geological studies show that the crustal shortening initiated in 3.5 Ma and has continued up to the present, reactivating the fault that was formed as a normal fault under an extensional stress field [*Sato,* 1994]. Therefore, it is interpreted that the mainshock fault plane of the mid-Niigata prefecture earthquake could be reactivated as a reverse fault in terms of the inversion tectonics [*Nakamura,* 1992]. Geological studies, however, have not estimated the extent of the depth of inversion tectonics. Based on the present study, it is suggested that the inversion tectonics initiated at great depths—at least 5–10 km—around the Niigata basin. The tomographic images associated with the inverted

normal fault are also observed at the EL Asnam fault zone and reveal the complex seismogenic structure as well as the mid-Niigata prefecture earthquake [*Chiarabba et al.,* 1997].

As shown in Figures 2b and 2c, the low V_p zone near the hypocenter of the mainshock may indicate the existence of high pore fluid pressures, low shear strength minerals, highly cracked rocks, etc. The low velocity zone near the hypocenter was also delineated in the case of the 1995 Kobe earthquake [*Zhao et al.,* 1996]. The low velocity zone can potentially initiate the mainshock rupture. The initiated rupture was propagated through the structural boundary between the low and high velocity bodies due to the relative mechanical weakness. In fact, the fault plane of the mainshock is an unfavorably oriented fault [*Sibson,* 1990] because the dip angle of the thrust fault is approximately 60° from the horizontal maximum compressional axis. Thus, the high pore fluid pressure or the low frictional coefficient within the fault zone (e.g., clay minerals) is required to reactivate the inverted normal fault.

Further, both the largest aftershock and the east-dipping aftershock occurred in the slightly low V_p zones, where the low-to-moderate V_p/V_s values are imaged (Fig. 2b, 3). According to *Takei* [2002], the relatively low V_p/V_s as well as the low V_p can be explained by the presence of water-filled pores with high aspect ratios. It is assumed that inhomogeneous distributions of the pore water contribute to the triggering of the aftershocks. We suggest that the sequence of aftershocks may be trigged by the loading of the shear stress released into the low velocity zones that are filled with pore water around the source region, where the seismic rupture is likely to be induced. It should be noted that the crustal stretching or shortening along the Japan coastline has created complex structures such as low velocity zones, which could control the seismic activities around the Niigata region.

Recent GPS (Global Positioning System) observations using the GEONET, operated by the Geographical Survey Institute, clarified that the source region is located at a significantly large E-W horizontal compressional area, which is termed the Niigata-Kobe Tectonic Zone (NKTZ) [*Sagiya et al.,* 2000]. Since many historical earthquakes occurred along the NKTZ, it can be argued that the

high strain rate affects the generation of large inland earthquakes. However, based on the present study, there remains the possibility that the high strain rate observed at the Niigata basin could be partially caused by the low elastic modules of the sediments extending to a depth of approximately 10 km. Thus, we need to separate the amount of surface deformation caused by the sediments from the observed strains. In addition, the sediments with low elastic modules can potentially indicate a ductile flow along the fault zone when the compression shear stress is applied. Since such ductile flow could play an important role in accumulating the shear stress on the source region, it is also important to consider the slow deformation in order to understand the generation of the large inland earthquake along the NKTZ.

We deployed about 50 seismic stations around the source region after the end of the immediate observations mentioned in this paper. In future, the seismic structure along the fault strike will be imaged in greater detail. The present study, however, is significant in providing the initial aftershock distributions and velocity structures in and around the source region immediately after the occurrence of the mainshock, and clarifying the crustal structure perpendicular to the fault strike.

Reference

Aki, K., Characterization of barriers on an earthquake fault, *J. Geophys. Res*., 84, 6140-6148, 1979.

Chiarabba, C., A. Amato, M. Meghraoui, Tomographic images of the EI Asnam fault zone and the evolution of a seismogenic thrust-related fold, *J. Geophys. Res.,* 102, 24485-24498, 1997.

Geological Survey of Japan, AIST, Gravity map of Japan, CD-ROM Version, Digital Geoscience Map P-2, 2000.

Geological Survey of Japan, AIST, Geological map of Japan, CD-ROM Version, Digital Geoscience Map G-3, 2002.

Hauksson, E., D. Oppenheimer, T. M. Brocher, Imaging the source region of the 2003 San Simoen earthquake within the weak Franciscan subduction complex, central California, *Geophys. Res. Lett.,* 31, L20607, doi:10.1029/2004GL021049.

Li, Y. G. and J. E. Vidale, Healing of the shallow fault zone from 1994 - 1998 after the 1992 M7.5 Landers, California, earthquake, *Geophys. Res. Lett.,* 28, 2999-3002, 2001.

Nakamura, K., Inversion tectonics and its structural expression (in Japanese with English abstract), *J. Tectonic Res. Group Jpn*., 38, 3-45, 1992.

Sagiya, T., S. Miyazaki, and T. Tada, Continuous GPS array and present-day crustal deformation of Japan, *Pure Appl. Geophys.,* 157, 2303-2322, 2000.

Sato, H., The relationship between late Cenozoic tectonic events and stress field and basin development in northeast Japan, *J. Geophys. Res.,* 99, 22261-22274, 1994.

Sibson, R. H., Rupture nucleation on unfavorably faults, *Bul. Seismol. Soc. Am.,* 80, 1580-1604, 1990.

Takeda T., H. Sato, T. Iwasaki, N, Matsuta, S. Sakai, T. Iidaka and A. Kato, Crustal structure in the northern Fossa Magna region, central Japan, from refraction/wide-angle reflection data, *Earth Planetary Science*, 56, 1293-1299, 2004.

Takei, Y., Effect of pore geometry on V_p/ V_s: From equilibrium geometry to crack, *J. Geophys. Res.,* 107, No. B2, 10.1029/2001JB000522, 2002.

Zhang, H., and C. H. Thurber, Double-difference tomography: The method and its application to the

Hayward fault, California, *Bul. Seismol. Soc. Am.,* 93, 1875-1889, 2003.

Zhao, D, A. Hasegawa, and S. Horiuchi, Tomographic imaging of P and S wave velocity structure

beneath northeastern Japan, *J. Geophys. Res.,* 97, 19909-19928, 1992.

Zhao, D., H. Kanamori, H. Negishi, D. Wiens, Tomography of the source area of the 1995 Kobe

earthquake: evidence for fluids at the hypocenter?, *Science*, 274, 1891–1894, 1996.

Depth(*km*)	Western side(*km/s*)	Eastern side(*km/s*)
0	2.30	2.30
3	4.05	5.91
6	5.72	5.93
9	5.81	5.95
12	5.89	5.98
15	5.97	6.00

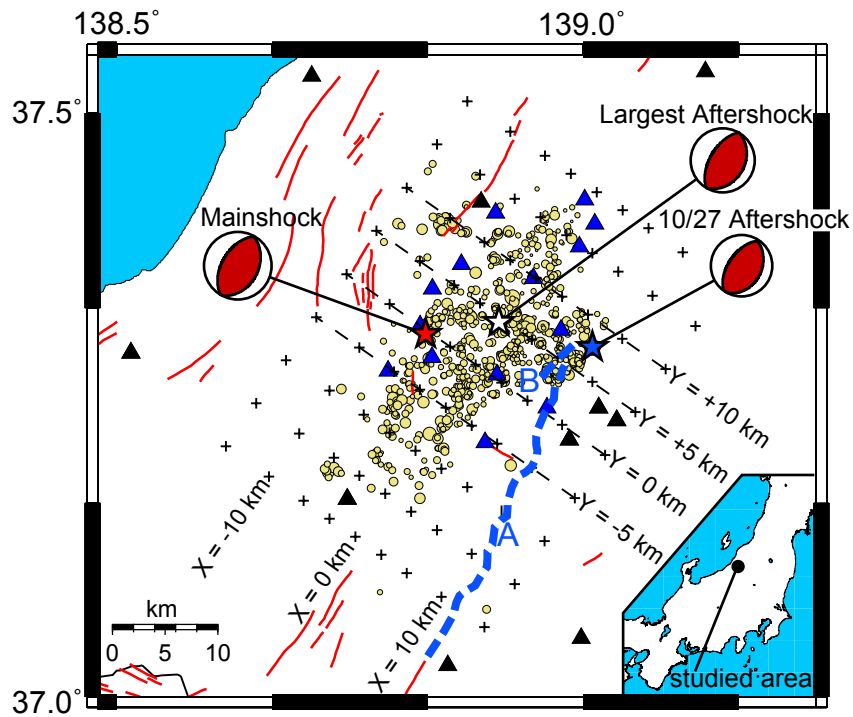Table 1. List of the initial velocity model for the tomography.

Figure 1. Maps of the relocated aftershock hypocenters determined in this study, shown as yellow circles scaled to the earthquake magnitude. The three stars denote the hypocenters of the mainshock, the largest aftershock ($M_w = 6.3$, Oct. 23) (relocated with the double difference data using the obtained velocity structure), and the $M_w = 5.8$ aftershock (Oct. 27), respectively, with the moment tensor from NIED. The blue and black triangles denote the temporary seismic stations and permanent stations, respectively. The grids used in the tomography (crosses) and horizontal lines (broken lines) for cross sections in Figure 2 are shown. The Muikamachi (A) and Obiro (B) faults are shown by blue broken lines, and the other major active faults are drawn as red lines.
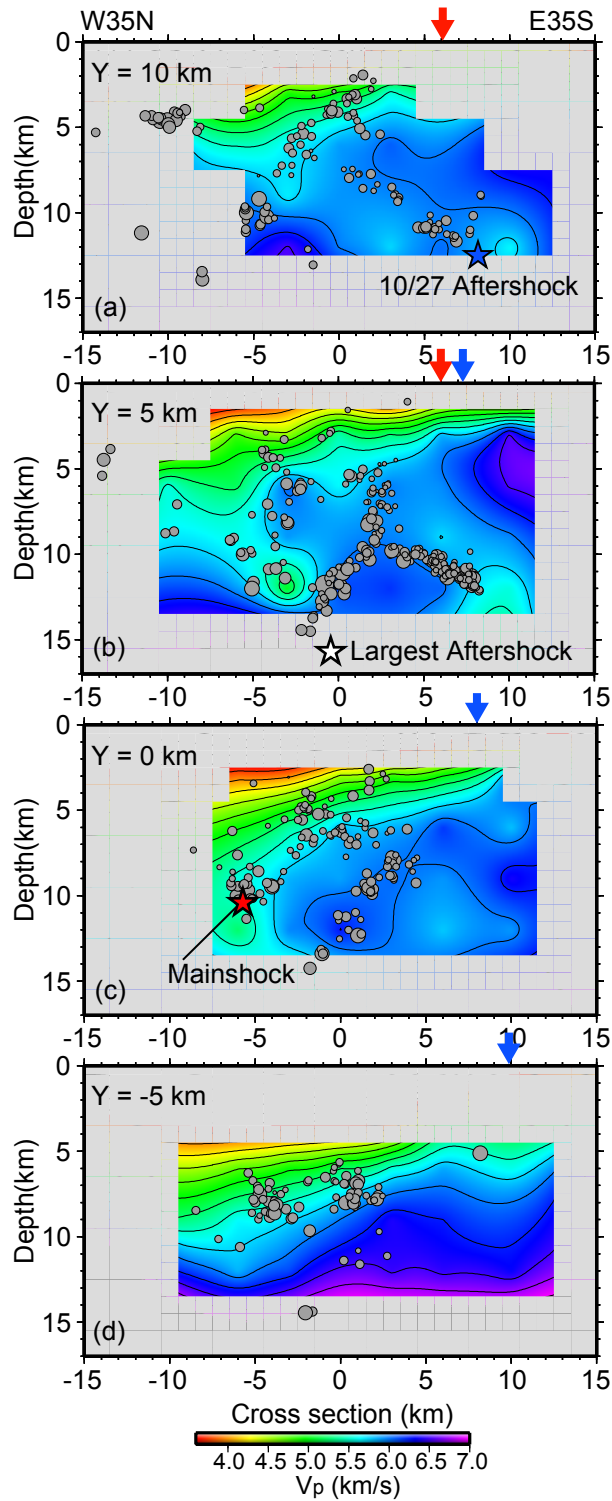
,

Figure 2. Four depth sections through the Vp model are shown along with the relocated aftershocks distributed within ± 2.5 km along each line shown in Figure 1. (a)Y=10 km, (b)Y=5 km, (c)Y=0 km, (d)Y= −5 km. The white-masked areas correspond to the low model resolution. The contour line interval is 0.25 km/s. The three stars denote the hypocenters of the mainshock, the largest aftershock (Oct. 23), and the Mw = 5.8 aftershock (Oct. 27), respectively. Red and Blue arrows at the top of each figure denote the approximate locations of the surface trace of the Obiro- and the Muikamachi-fault.
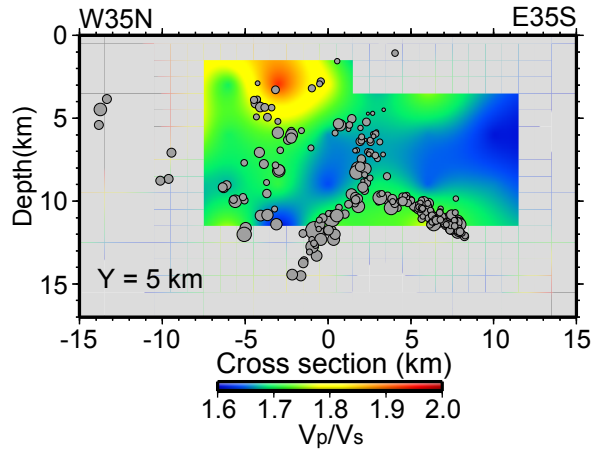
Figure 3. The depth sections of the $V_{\mathrm{p}}/V_{\mathrm{s}}$ structure along the Y = 5 km cross-section are shown along with the relocated aftershocks.